Materials Horizons

ROYAL SOCIETY OF CHEMISTRY

COMMUNICATION

View Article Online
View Journal | View Issue

Cite this: *Mater. Horiz.*, 2023, **10**, 1309

Received 9th August 2022,
Accepted 9th January 2023

DOI: 10.1039/d2mh00984f

rsc.li/materials-horizons

Directly measuring flexoelectric coefficients μ_{11} of the van der Waals materials†

Menghan Deng,[a] Xiang Wang,[a] Xionghu Xu,[a] Anyang Cui, *[a] Kai Jiang,[a] Jinzhong Zhang, [a] Liangqing Zhu,[a] Liyan Shang,[a] Yawei Li, [a] Zhigao Hu *[ab] and Junhao Chu[ab]

Flexoelectricity originates from the electromechanical coupling interaction between strain gradient and polarization, broadly applied in developing electromechanical and energy devices. However, the study of quantifying the longitudinal flexoelectric coefficient (μ_{11}) which is important for the application of atomic-scale two-dimensional (2D) materials is still in a slow-moving stage, owing to the technical challenges. Based on the free-standing suspension structure, this paper proposes a widely applicable method and a mensurable formula for determining the μ_{11} constant of layer-dependent 2D materials with high precision. A combination of *in situ* micro-Raman spectroscopy and piezoresponse force microscopy (PFM) imaging was used to quantify the strain distribution and effective out-of-plane electromechanical coupling, respectively, for μ_{11} constant calculation. The μ_{11} constants and their physical correlation with the variable mechanical conditions of naturally bent structures have been obtained extensively for the representative mono-to-few layered MX_2 family (M = W and Mo; X = S and Se), and the result is perfectly consistent with the estimated order-of-magnitude of the μ_{11} value (about 0.065) of monolayer MoS_2. The quantification of the flexoelectric constant in this work not only promotes the understanding of mechanical and electromechanical properties in van der Waals materials, but also paves the way for developing novel 2D nano-energy devices and mechanical transducers based on flexoelectric effects.

New concepts

The study of quantifying the longitudinal flexoelectric coefficient (μ_{11}) is significant for the application of flexoelectricity in flexible materials, but still in a slow-moving stage. A widely applicable method and a mensurable formula to determine the μ_{11} constant of any two-dimensional (2D) materials are proposed in this study. The μ_{11} coefficient of the representative MX_2 family has been experimentally obtained for the first time with high precision. Along the way, we further explored the mechanical property dependent μ_{11} constant, which can be modulated by changing the thickness of 2D films. The present study provides ground-breaking and clear results on the flexoelectricity effect of functional 2D materials. It promotes the understanding of mechanical and electromechanical coupling properties of van der Waals material and paves the way for developing energy devices based on flexoelectricity.

Electromechanical coupling is widely applied in electronic engineering fields as one of the most famous methods of converting mechanical deformation into electrical energy.[1,2] Studies on electromechanical coupling in nanomaterials, and particularly two-dimensional (2D) materials such as graphene and MoS_2 have mainly focused on their piezoelectric properties,[3–9] but ignored the flexoelectric effect. Generally, piezoelectricity is limited to materials with non-centrosymmetric crystal structures. Flexoelectricity, *i.e.*, electric polarization induced by strain-gradient, is the central reason that explains the emergence of apparent out-of-plane piezoelectric response in bent atomically thin 2D materials.[10] In comparison with piezoelectricity, the flexoelectric response depends more easily on the strain gradient, and has broader applications in diverse material systems.[11,12] Nevertheless, the flexoelectric properties of 2D materials remain unexplored to great extents. Especially, the study of quantifying the longitudinal flexoelectric coefficient (μ_{11}) is still in a slow-moving stage, owing to the technical challenges and the undefined physical structure. It is difficult to establish a suitable theoretical model of few-layer atoms for theoretical calculations, with complex interlayer interactions among the multi-layer atoms. In terms of experimental observations, it is very challenging to

[a] *Technical Center for Multifunctional Magneto-Optical Spectroscopy (Shanghai), Engineering Research Center of Nanophotonics Advanced Instrument (Ministry of Education), Department of Physics, School of Physics and Electronic Science, East China Normal University, Shanghai 200241, China.*
E-mail: aycui@phy.ecnu.edu.cn, zghu@ee.ecnu.edu.cn; Fax: +86-21-54342933; Tel: +86-21-54345150

[b] *Collaborative Innovation Center of Extreme Optics, Shanxi University, Taiyuan, Shanxi 030006, China*

† Electronic supplementary information (ESI) available: analytical derivations regarding the stress gradient in the z direction; relevant components of the elasticity matrixes of MX_2 films; flexoelectric polarization and nonuniform strain quantification of monolayered to few-layered MoS_2, $MoSe_2$, WS_2, WSe_2 flakes. See DOI: https://doi.org/10.1039/d2mh00984f

simultaneously effectively induce the flexoelectric effect and quantify the strain gradient of the films non-destructively. Therefore, a reliable method to obtain the μ_{11} constant of mono-to-few layered 2D material films has not been discovered so far.

Recently, flexoelectric properties of 2D materials have been preliminarily studied by means of density functional theory (DFT) calculations and piezoresponse force microscopy (PFM) technology. Kalinin *et al.* have confirmed a linear correlation between the induced dipole moment and bending curvature in graphene by DFT.[13] The theoretical analysis of flexoelectricity in carbon nanostructures helped establish the universality of linear dependence of flexoelectric atomic dipole moments on local curvature.[14] Zhuang *et al.* employed an atomistic model to account for charge–dipole interactions, and reported the intrinsic flexoelectric constants for 2D materials.[15,16] Suryanarayana *et al.* performed symmetry-adapted DFT simulations to calculate transversal flexoelectric coefficients along the principal directions in fifty-four selected atomic monolayers.[17,18] Brennan *et al.* obtained an order-of-magnitude estimate of flexoelectric coefficients of monolayer WS_2, WSe_2, MoS_2 and $MoSe_2$ films.[5,19] In addition, a primary method has been proposed in our recent work to quantify the effective out-of-plane electromechanical coupling response induced by strain gradient in the curved films using PFM.[10] At present, most research studies on flexoelectric properties of 2D materials, specifically determining the flexoelectric coefficients are in the stage of theoretical prediction for a single atomic layer. The direct measurement of flexoelectric coefficients in 2D films is difficult due to the technical restriction of and ambiguity in the strain-gradient effect induced by substrates for supported 2D systems. And some negative effects would be inevitably imposed by the substrates, such as clamping effects, parasitic charges, and doping effects.[20–22] In the measurement of flexoelectric coefficients, the complicated substrate effects can induce a net strain (and hence parasitic piezoelectricity) in addition to strain gradients and flexoelectricity, resulting in unexpectable experimental error results. Therefore, due to theoretical and technical restrictions, the study on flexoelectric constants of 2D materials with polyatomic stacks have not been carried out yet. The μ_{11} coefficients of mono-to-few layered 2D material films have never been quantified experimentally. The inadequate understanding of flexoelectric properties has greatly hindered the development and application of flexible devices based on the layered semiconductors. Therefore, we are particularly looking forward to a reliable and accurate approach to directly quantify the μ_{11} coefficient of atomically thin materials.

In this work, a suspended atomic layered structure is designed to induce the flexoelectric effect on free-standing 2D materials. The utilization of suspended structures not only helps achieve large deformation but also could help effectively avoid the substrate effects so as to accurately determine the μ_{11} coefficient of 2D flakes. Based on this suspension structure, we have novelly proposed a general formula to directly quantify the μ_{11} coefficients, taking MX_2 (M = W and Mo; X = S and Se) flakes as the representatives of 2D materials. According to the formula, we have experimentally measured the μ_{11} coefficient of 2D materials by the *in situ* micro-Raman spectroscopy and PFM imaging methods. Following the distribution of the stress gradient and the effective out-of-plane piezoelectric coefficient (d_{33}^{eff}), the μ_{11} coefficient of monolayer curved films is determined. Notably, the μ_{11} coefficient of monolayer bent MoS_2 flakes is determined to be approximately 0.061 μC m^{-1}. This result agrees well with the previously reported estimates for the order-of-magnitude, proving the accuracy of formula derivation. Moreover, it is highly suitable for achieving the μ_{11} constant of layer-dependent 2D materials. Here, we have first obtained the μ_{11} constants of bent layer-dependent WS_2, WSe_2, MoS_2 and $MoSe_2$. Note that, the physical effects of film thickness and aspect ratios on the μ_{11} coefficient are further qualitatively discussed. Our work gives a physical method and mechanical origins for quantifying flexoelectric properties in 2D materials and paves the way for the design of flexoelectricity based nano-electromechanical applications.

The paper is structured as follows: the result section consists of five parts. The general formula for calculating μ_{11} coefficients of 2D materials is proposed in former two parts. Taking the curved monolayer MoS_2 film as an example, the nonuniform strain distribution and strain gradient of free-standing monolayer 2D flakes are quantitatively studied in the third part. In the fourth part, flexoelectric polarization induced by the strain gradient in monolayer MX_2 flakes was observed and quantified. Meanwhile, combining the strain and d_{33}^{eff} coefficient distribution, μ_{11} coefficients of monolayer bent MX_2 flakes were further determined using the general formula. The last part gives the solution process of the μ_{11} coefficient of few-layered MX_2 films, and the factors influencing the μ_{11} coefficient are qualitatively discussed.

Strain evaluation of curved 2D films

The suspended structure as a typical model for studying the strain effect can effectively prevent the substrate effects and yield large deformation in transition metal dichalcogenide (TMDs) flakes.[23,24] Fig. 1a presents the schematic illustration of the TMD films bending naturally over the hole. Fig. 1b displays the three-dimensional (3D) morphological image of the suspended 2D films, showing the principal components of the strain tensor, along the circumferential (ε_t) and radial (ε_r)

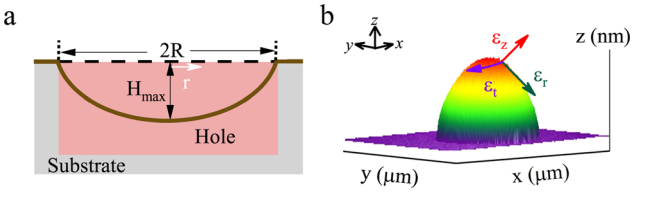

Fig. 1 (a) Schematic of the bending film naturally over the hole. The radial coordinate along the hole diameter is defined as *r*, where $r = 0$ at the center of the hole. The hole diameter is 2*R*, and the maximum depth of curved films is H_{max}. (b) 3D AFM data of suspended 2D flakes, with the marked components of the strain tensor along three principal axes. The solid red arrow represents the perpendicular component (ε_z) of strain. Green and purple ones represent the radial (ε_r) and the circumferential component (ε_t), respectively.

Table 1 Poisson's ratio (ν) of MX_2 flakes

Material	WS_2	WSe_2	$MoSe_2$	MoS_2
(ν)	0.217	0.192	0.239	0.249

in-plane directions[25] and the perpendicular (ε_z) out-of-plane directions. For the suspended flakes, the biaxial strain is isotropic ($\varepsilon_t = \varepsilon_r$) only at the bottom of the bent films and reaches its maximum.[26] As the circumferential component (ε_t) tends to zero near the hole's edge, the in-plane strain gradually becomes uniaxial. Thus, the bending film is characterized by an anisotropic in-plane strain, which increases from the edge to the bottom.[26–28] Because the outline of the suspended films is spherically symmetrical,[26] the radial (ε_r) and circumferential (ε_t) components have identical effects on the electronic properties of TMDs.[29] In order to quantify the strain in the suspended films, the anisotropic strain tensor is translated into a total in-plane strain defined as $\varepsilon_p = \varepsilon_r + \varepsilon_t$.[27] Following Hencky's model,[23,30] the total in-plane strain at the bottom of suspended films can be expressed as:[26]

$$\varepsilon_p^{bottom} = 2 \cdot f(\nu) \cdot \left(\frac{H_{max}}{R}\right)^2 = 2 \cdot \left(\frac{H_{max}}{R}\right)^2 \cdot \frac{b_o(\nu)(1-\nu)K(\nu)^{2/3}}{4} \quad (1)$$

where H_{max} and R are the bending depth and radius of holes, respectively. $b_o(\nu)$ and $K(\nu)$ are variables that only depend on Poisson's ratio (ν). The values of ν for MX_2 flakes are listed in the following Table 1.[31] For MX_2 flakes, the exact values of b_o and K can be evaluated by numerical methods of interpolation analysis. We perform interpolation between the values reported in the literature,[23,32] from which $f(\nu)$ of all compounds is finally obtained. The values of $b_o(\nu)$, $K(\nu)$, and $f(\nu)$ are presented in the Table 2. Thus, the total in-plane strain at the bottom of the suspended flakes can be further quantified.

The formula for calculating the μ_{11} coefficients

For bulk dielectric materials, d_{33}^{eff} generated by the flexoelectric effect can be expressed as[15,16,33,34]

$$d_{33}^{eff} = \mu_{11}\frac{\nabla_z T_z}{c_{11} T_z'} \quad (2)$$

where μ_{11} is the longitudinal flexoelectric coefficient of a dielectric material, c_{11} is the elastic coefficient, $\nabla_z T_z$ is the stress gradient in the z-axis direction, and T_z' is the stress along the z-axis, respectively.

Table 2 b_o, K, and $f(\nu)$ values of MX_2 films

Material	WS_2	WSe_2	$MoSe_2$	MoS_2
b_o	1.689	1.680	1.698	1.702
K	3.274	3.192	3.350	3.386
$f(\nu)$	0.729	0.736	0.725	0.721

Note that eqn (2) is applied to the calculation of the flexoelectric effect of curved films, and it needs to be further modified. Both μ_{11} and c_{11} are constants, for the bent flakes whose hole radius and bending depth are definite. Thus, the value of d_{33}^{eff} is proportional to the ratio of stress gradient and stress along the z-axis. For biaxially strained TMDs, the out-of-plane component of the strain tensor can be written as[35]

$$\varepsilon_z = -\frac{D_{13}}{D_{33}}(\varepsilon_r + \varepsilon_t) = -\frac{D_{13}}{D_{33}}\varepsilon_p \quad (3)$$

where D_{13} and D_{33} are the pertinent components of the elasticity matrix. We adopted the following anisotropic elasticity matrixes.[36,37] (all units: GPa)

For MoS_2,

$$D = \begin{pmatrix} 178 & 45 & 1 & 0 & 0 & 0 \\ 45 & 178 & 1 & 0 & 0 & 0 \\ 1 & 1 & 3 & 0 & 0 & 0 \\ 0 & 0 & 0 & 1 & 0 & 0 \\ 0 & 0 & 0 & 0 & 1 & 0 \\ 0 & 0 & 0 & 0 & 0 & 67 \end{pmatrix}$$

For WSe_2,

$$D = \begin{pmatrix} 158 & 31 & 1 & 0 & 0 & 0 \\ 31 & 158 & 1 & 0 & 0 & 0 \\ 1 & 1 & 2 & 0 & 0 & 0 \\ 0 & 0 & 0 & 1 & 0 & 0 \\ 0 & 0 & 0 & 0 & 1 & 0 \\ 0 & 0 & 0 & 0 & 0 & 64 \end{pmatrix}$$

For WS_2,

$$D = \begin{pmatrix} 196 & 43 & 1 & 0 & 0 & 0 \\ 43 & 196 & 1 & 0 & 0 & 0 \\ 1 & 1 & 3 & 0 & 0 & 0 \\ 0 & 0 & 0 & 1 & 0 & 0 \\ 0 & 0 & 0 & 0 & 1 & 0 \\ 0 & 0 & 0 & 0 & 0 & 76 \end{pmatrix}$$

For $MoSe_2$,

$$D = \begin{pmatrix} 146 & 34 & 1 & 0 & 0 & 0 \\ 34 & 146 & 1 & 0 & 0 & 0 \\ 1 & 1 & 3 & 0 & 0 & 0 \\ 0 & 0 & 0 & 1 & 0 & 0 \\ 0 & 0 & 0 & 0 & 1 & 0 \\ 0 & 0 & 0 & 0 & 0 & 56 \end{pmatrix}$$

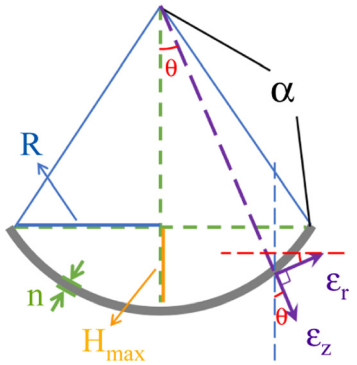

Fig. 2 Schematic diagram of bent flakes. Definitions of each parameter are given in the diagram.

Thus, the perpendicular strain component of MoS_2, WS_2, and $MoSe_2$ can be written as $\varepsilon_z = -\frac{1}{3}(\varepsilon_r + \varepsilon_t) = -\frac{1}{3}\varepsilon_p$. Similarly, for WSe_2, $\varepsilon_z = -\frac{1}{2}(\varepsilon_r + \varepsilon_t) = -\frac{1}{2}\varepsilon_p$.

The schematic diagram of bent films and definition of each parameter for calculation are given in Fig. 2. The strain along the z-axis is defined as $\varepsilon_\perp$, where for 2D flakes, it follows

$$\varepsilon_\perp = \varepsilon_z \cos\theta - \varepsilon_r \sin\theta \quad (4)$$

At the hole edges, $\cos\theta = \frac{\alpha - H_{max}}{\alpha}$. According to the Pythagorean theorem, the radius of curvature α may be written as $\alpha = \frac{{H_{max}}^2 + R^2}{2H_{max}}$. The curvature is the inverse of the radius of curvature. Since $\alpha \gg H_{max}$, we obtain approximately $\cos\theta \approx 1$. From the hole edge to the center, θ gradually decreases to zero, while $\cos\theta$ increases to 1 by degrees. Hence, for the whole curved area, the z-axis component of the radial strain (ε_r) could be ignored. Furthermore, the strain along the z-axis can be estimated from the strain component (ε_z) in the out-of-plane direction. For free-standing 2D flakes, substituting $\varepsilon_z = -\frac{D_{13}}{D_{33}}\varepsilon_p$ into eqn (2), the d_{33}^{eff} constant is obtained as

$$d_{33}^{eff} = \frac{\mu_{11}}{c_{11}} \frac{\frac{\partial \varepsilon_p}{\partial z}}{\varepsilon_p}. \quad (5)$$

The calculation method of $\frac{\partial \varepsilon_p}{\partial z}$ is given in the ESI.† According to the experimental results, the curvature of thin-layered flakes (K) is approximately equal to strain gradient, $\frac{\partial \varepsilon_p}{\partial z} \approx K = \frac{1}{\alpha}$. This result is in good agreement with the conclusion obtained by molecular dynamics simulations in the mechanical bending model.[15,16] Hence, the universal formula for calculating the flexoelectric coefficient of curved 2D materials can be further simplified as

$$\mu_{11} = \frac{c_{11} d_{33}^{eff} \varepsilon_p}{\frac{\partial \varepsilon_p}{\partial z}} = \alpha d_{33}^{eff} c_{11} \varepsilon_p. \quad (6)$$

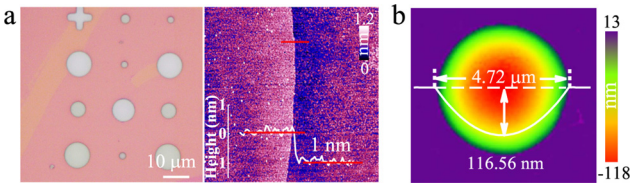

Fig. 3 (a) Optical and AFM images of monolayer MoS_2 on porous substrates. The height profile along the red line is shown in the inset of the right topographic map. (b) AFM topography image of suspended monolayer MoS_2. The inset shows the scan height map along the diameter of holes.

Based on the proposed general eqn (6), the μ_{11} constants of free-standing monolayer/few-layered MX_2 flakes are quantified for the first time in this work.

Nonuniform strain quantification

As shown in Fig. 1a, the TMD films bend naturally over the hole. The thickness of few-layered 2D flakes was evaluated from the surface topographies. Fig. 3a presents the atomic force microscopy (AFM) topography and the optical image of a perforated substrate covered with monolayer MoS_2 flakes. The thickness of monolayer MoS_2 was determined to be about 1.0 nm. The topographic map of MoS_2 flakes suspended over a single hole is shown in Fig. 3b, in which the inset depicts the line profile along the diameter of the hole with a diameter of 4.72 μm. The MoS_2 film naturally bends in the suspended area, analogous to a circular arc shape with a depth of 116.56 nm. It confirms that the suspended flake is continuous and undamaged.

First, the biaxial strain distribution of bent monolayer MoS_2 was quantified by micro-Raman spectroscopy. For the unstrained monolayer MoS_2 films, Raman spectra show two characteristic peaks of the A_{1g} mode at 404 cm^{-1} due to out-of-plane vibrations, and the doubly degenerate E_{2g} mode at 385 cm^{-1} intrinsically from in-plane vibrations of the crystals. Fig. 4a displays the intensity mapping images around the bands of the E_{2g} mode. Compared with flat regions, the scattering intensity in the curved areas is larger. The variation of the scattering intensity is attributed to the strain dependence of the static dielectric function.[38] In the Placzek approximation, the non-resonant scattering intensities are expressed as:[39,40] $I(\nu) \propto |\vec{e}_s \cdot G(\nu) \cdot \vec{e}_i|^2 \frac{n_\nu + 1}{\omega_\nu}$, where $\vec{e}_i(\vec{e}_s)$ is the polarization vector of the incident (the scattered) laser, n_ν is the νth phonon occupation number at temperature T, and $G(\nu)$ is the Raman tensor. Under identical test conditions, the scattering intensity is positively correlated with the Raman tensor. In addition, $G(\nu)$ is in connection with the strain dependence of the static dielectric function. The increase in scattering intensity in the curved regions is attributed to the enhancement of the static dielectric function. The presence of compressive strain in the curved regions results in a greater static dielectric function, which in turn leads to an enhancement in Raman intensity. The influence of biaxial strain on TMD films is also reflected in the shift of the peak position of phonon modes. The peak position

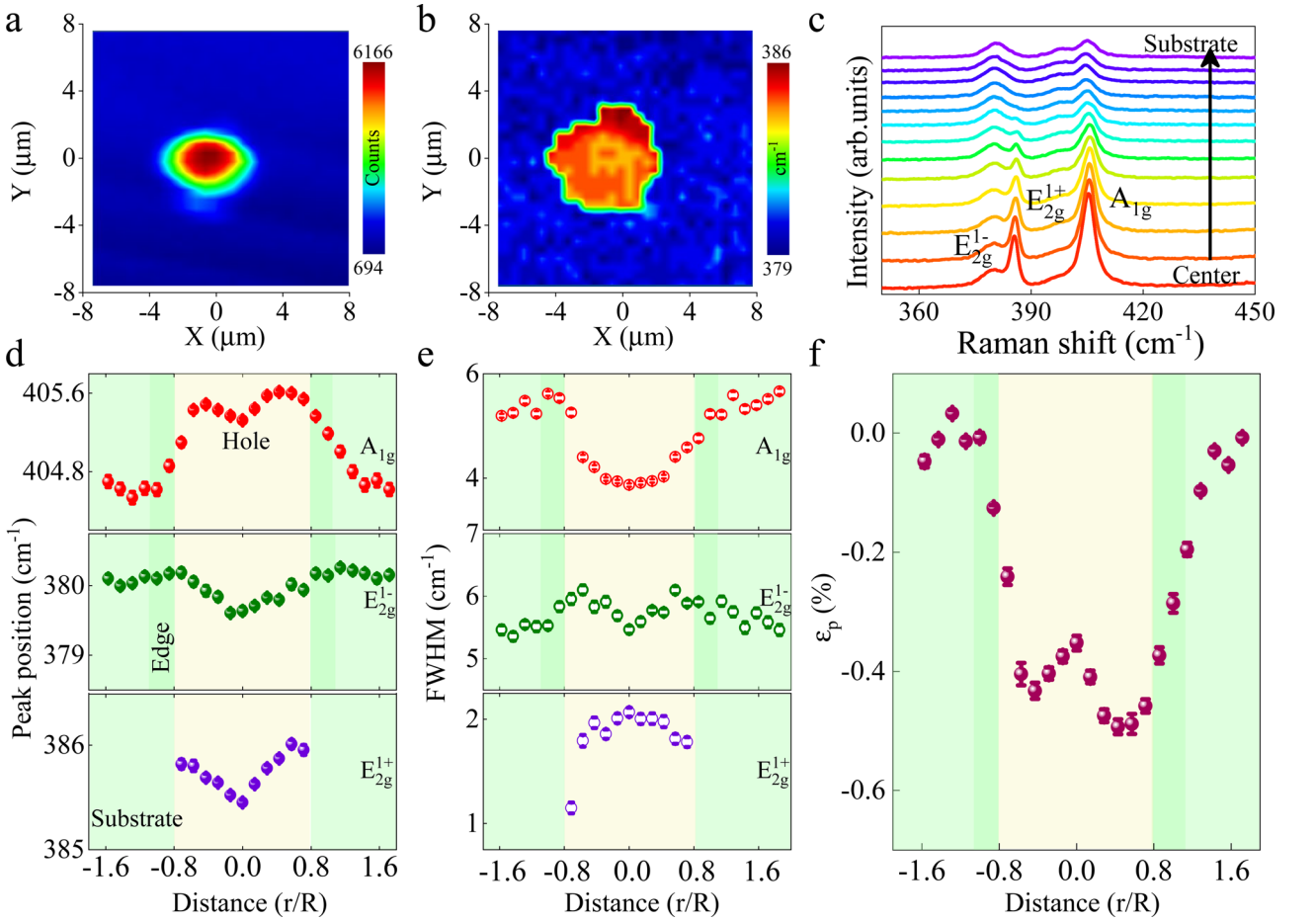

Fig. 4 E_{2g} Raman mode (a) intensity and (b) peak position mapping images of a suspended monolayer MoS_2 film. (c) Set of Raman spectra from the center to the right edge along the diameter of holes. (d and e) Raman peak positions, full width at half-maximum of both E^{1+}_{2g} E^{1-}_{2g} and A_1g as functions of r/R. (f) Strain distribution as functions of r/R.

mapping image of the E_{2g} mode is shown in Fig. 4b. On flat MoS_2, there are slight fluctuations in peak positions, which is caused by the rough substrate. Distinctly, an obvious peak shift can be seen between the curved and flat MoS_2 regions, which is intrinsically induced by the existence of local non-uniform strain. The E_{2g} phonon softens continuously from the edge to the center, indicating that the local strain continuously varies. A series of Raman spectra from the center to the right edge along the diameter of holes are shown in Fig. 4c. The double degenerate E_{2g} mode shows a red shift trend and splits into two peaks, while the A_{1g} mode presents a blue shift trend. The reason for the split of the E_{2g} mode is that the strain breaks the the symmetry of the hexagonal lattice. Since the strain worsens the symmetry of the system, the vibration mode of the curved MoS_2 film no longer originates from E_{2g}. The reason for the differences in trends of peak shifts between E_{2g} and A_{1g} modes will be further discussed.

In order to investigate the shift in the peak position more intuitively, the Lorentzian function was used to model E_{2g} and A_{1g} mode bands. Fig. 4d presents the peak positions obtained by Lorentz fitting as a function of r/R. Obviously, E_{2g} and A_{1g} modes show diverse peak-shift trends along the hole diameter from the edge to center. This phenomenon may be attributed to the different sensitivity to in-plane strain components. According to the membrane analysis method,[41] the two components of in-plane strain can be written as:

$$\varepsilon_r = \frac{2H_{max}^2}{R^2}\cdot\left(\frac{r}{R}\right)^2 - \frac{2u_0}{R}\cdot\left(\frac{r}{R}\right) + \frac{u_0}{R}$$
$$\varepsilon_t = -\frac{u_0}{R}\cdot\frac{r}{R} + \frac{u_0}{R} \quad (7)$$

where $0 \le \frac{r}{R} \le 1$. For a bent film of measured radius and bending depth, the parameter u_0 is constant and depends only on Poisson's ratio. The circumferential strain decreases linearly from the center to the edge, while the radial strain presents a nonlinear trend and first minishes and then increases. The frequency of A_{1g} and E_{2g} modes is negatively correlated with the biaxial strain of monolayer MoS_2 films.[23] For phonons that are sensitive to the radial strain component, a nonlinear trend would be observed: first an increase and then a decrease from the center to the edge. This is in accordance with the frequency variation of the A_{1g} mode. Consequently, it would be concluded that A_{1g} and E_{2g} modes become sensitive to the radial strain

and the circumferential one, respectively. For MoS_2, we take the value of Poisson's ratio to be $\nu = 0.249$, leading to $f(\nu) = 0.721$. Therefore, the biaxial strain at the center of the bent monolayer MoS_2 film is $\varepsilon_p^{bottom} = 0.35\%$. Two single-line subbands are observed, due to the splitting of the double degenerate optical E_{2g} phonon mode. We define the lower and higher frequency splitting modes as E_{2g}^{1-} and E_{2g}^{1+}, respectively. Assuming linear dependence of the frequencies on the biaxial strain, the shift rates of the A_{1g}, E_{2g}^{1-}, and E_{2g}^{1+} modes for monolayer MoS_2 are obtained to be -2.07, -1.32, and $-5.0\ cm^{-1}\ \%^{-1}$, respectively. The results are in agreement well with the reported values,[23,42,43] indicating that the biaxial strain induces the mode softening linearly with strain, as expected. Furthermore, using the formula[44] $\gamma = [\omega - \omega_0]/[2\varepsilon\omega_0]$, where ω_0 and ω are phonon frequencies under no strain and finite strain, respectively, we calculate the Grüneisen parameters of phonons to be $\gamma_{A1g} = 0.26$, $\gamma_{E_{2g}^{1-}} = 0.17$ and $\gamma_{E_{2g}^{1+}} = 0.65$.

Furthermore, the full width at half-maximum (FWHM) could qualitatively reflect the inhomogeneity of nanoscale strain.[45] The FWHM value as a function of r/R is depicted in Fig. 4e. FWHM of A_{1g} and E_{2g} modes symmetrically distributes from the center, indicating the symmetrical distribution of local strain. The FWHM of E_{2g} mode varies linearly from the center to the edge, while the FWHM of A_{1g} is nonlinear. It illustrates the local inhomogeneous strain. The unusual variation trends of the two phonon modes are attributed to the fact that A_{1g} and E_{2g} modes are more sensitive to the radial strain and circumferential component, respectively. Compared with the E_{2g} mode, the A_{1g} mode is weakly affected by uniaxial strain and more sensitive to biaxial strain.[43,46] Therefore, the frequency variation of the A_{1g} mode could more accurately reflect the biaxial strain distribution of the bent film. Fig. 4f summarizes the strain distribution obtained by A_{1g} frequency evolution. The presence of a slight strain near the hole indicates that the bent films could influence the surrounding supported MoS_2 film. The total in-plane strain (ε_p) of the monolayer curved MoS_2 film varies in a nonlinear and continuous manner, which is analogous to the variation of the radial strain component (ε_r) from the center to the edge. Furthermore, the ε_p distribution and basic characterization of monolayer WSe_2, WS_2, and $MoSe_2$ flakes are further presented in Fig. S1–S4 (ESI†). Similarly, the ε_p of monolayer WS_2, WSe_2, and $MoSe_2$ films also shows a nonlinear continuous variation trend.

In addition, the evolution of the electronic structure in the same sample under strain has been investigated by photoluminescence (PL) spectroscopy. Fig. 5a presents the PL spectra collected from edges to the center of the hole along its diameter direction. As the strain increases, the FWHM of PL decreases while the emission intensity enhances appreciably. The significant increase in the PL intensity indicates an enhancement of light emission efficiency.[47] When strain is applied, the band structure of MoS_2 is modified, resulting in an augmentation of the density of carriers. The accession in the number of carriers leads to an escalation in the radiative recombination of carriers, which in turn improves the PL intensity. The peak position and energy from PL emission as the function of r/R

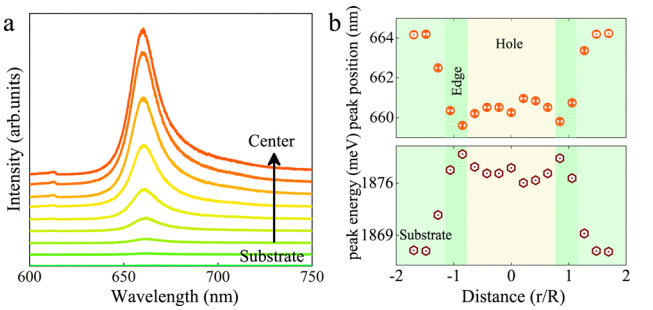

Fig. 5 (a) PL spectra of bent monolayer MoS_2 from the left edge to the center of a hole along its diameter direction. (b) PL peak position (upper) and peak energy (bottom) with respect to the r/R value.

have been plotted in Fig. 5b. Due to the presence of strain, the PL peak energy enhances from the hole vicinity. From the edge to the center, the PL peak energy presents a nonlinear trend and decreases first and then goes up, which is consistent with the in-plane total strain trend shown in Fig. 4f. Compared with the flat region, the PL emission peaks in the bent region shifted significantly to higher energy. This phenomenon results from the fact that the direct energy gap of monolayer MoS_2 is changed by biaxial compressive strain. Monolayer MoS_2 has a direct band gap (E_{dir}), which is determined from the difference between the valence band maximum (VBM) and the conduction band minimum (CBM) at the K point. The applied compressive strain would bring about a larger S–Mo–S bond angle. In this case, the coupling between the p orbital and d_{z^2} orbital enhances, while the coupling between the p and in-plane orbital weakens.[48] Thus, the CBM and VBM shift to higher and lower energies, respectively. The energy shift in the opposite direction leads to an increase in the direct band gap, which in turn pushes the PL emission peak to higher energy. When a total in-plane strain of 0.35% is applied, the peak energy shift is about 9.2 meV, according to 3.9 nm in wavelength variation.

Determining longitudinal flexoelectric constants

Recently, PFM has gradually become an indispensable tool to investigate local piezoelectric and ferroelectric properties in diverse material systems. The apparent piezoresponse signal in PFM may result from many distinct microscopic mechanisms other than the piezoelectric effect, such as flexoelectricity, electrostriction, electrostatic effect, electrochemical strain, *etc.*[49–53] Because of the presence of an electrostatic potential difference between the AFM tip/cantilever and the sample surface, *i.e.*, the surface potential, the electrostatic interaction can readily exist. The electrostatic interaction can be the most important factor among several non-piezoelectric contributions to PFM measurements due to the intrinsic nature of the surface potential. Kim *et al.* examined the impact of the electrostatic effect on the electromechanical response in PFM and explored ways to minimize the electrostatic effect.[53–56] Among them, the electrostatic effect can be easily evaluated by the measurement

of surface potential. For materials with relatively lower surface potential (around a few hundreds of millivolts), the electrostatic effect induced by the surface potential was not significant. In our work, Kelvin probe force microscopy (KPFM) was used to evaluate the surface potential of MX_2 films. In principle, surface potential measured directly by the KPFM method is the contact potential difference between the tip and sample. The voltage is applied to the tip in our experiment. Under the circumstances, the contact potential difference (V_{CPD}) can be written as:

$$V_{CPD} = \frac{\Phi_{tip} - \Phi_{sample}}{e} \quad (8)$$

where Φ_{tip} is the work function of the tip, Φ_{sample} is the work function of the sample, and e is the elementary charge. First, we measured the surface potential of different samples, as shown in Fig. S5 (ESI†). The KPFM results showed that the relatively lower surface potential of supported MoS_2, $MoSe_2$, WS_2, and WSe_2 films are −234 mV, 157 mV, 35 mV, and 344 mV, respectively. Furthermore, the surface potential measurements of monolayer MoS_2 with various bending states are depicted in Fig. S6 (ESI†). A decrease in the surface potential, compared to that of the supported area, was clearly observed in the curved region. The difference in surface potential between the suspended and supported area is defined as ΔV_{CPD}, *i.e.*, $\Delta V_{CPD} = V_{CPD\text{-suspended}} - V_{CPD\text{-supported}}$. With an increase in strain (0.086–0.59%), ΔV_{CPD} increased from 70 mV to 470 mV. The decreased surface potential of the curved region originates dominantly from the increase in work function induced by strain.[57] Overall, the surface potential of the sample fluctuated between several hundreds of millivolts, which is relatively low. The PFM response was not significantly affected by the electrostatic effect induced by surface potentials of a few hundreds of millivolts. Therefore, the electrostatic effect can be ignored during our PFM measurement.

The inhomogeneous strain distribution on the bent film leads to a strain gradient along the out-of-plane direction, which can induce flexoelectricity by breaking the crystallographic inversion symmetry.[33,34,58,59] MoS_2 comprises a triple atomic layer structure, in which each central Mo atom bonds with the upper and lower sulphur atoms. For a single atomic layer, nonzero dipole moments are also induced into each atom due to the nonzero z component of the interatomic distance. Due to the equidistant separation with the central Mo atoms, an equal and opposite dipole moment is observed for the top and bottom sulphur atoms, while no dipole moment is found for Mo atoms due to the symmetric configuration. At this time, the net dipole moment is zero. The imposed bending deformation induces varied deformations of the top and bottom sulphur layers relative to the central atom. After bending, there is a compression in the bond lengths between Mo and S atoms in the layers above, while the bond length with the bottom sulphur layers is stretched.[15] However, the existence of a strain gradient contributes the stretching ond compression of bond lengths for each Mo atom to various extents. The deviation in bond length breaks the symmetry of undeformed MoS_2, which results in nonzero net dipole moments. The existence of the nonzero dipole moment then produces flexoelectric polarization. Flexoelectricity is the central reason for the emergence of apparent out-of-plane piezoelectric response in bent atomically thin 2D materials. In this work, the flexoelectric effect induced by the strain gradient in the suspended structure is the main reason for the appearance of a strong out-of-plane piezoelectric signal in PFM.

In order to reveal the effective out-of-plane electromechanical coupling induced by the strain gradient on bent MoS_2 flakes, *in situ* PFM was used to measure the same sample. Piezoelectric measurements were performed in the contact mode with an alternating current (AC) signal (drive excitation) applied to the conducting AFM tip at a frequency of 15 kHz, selected to be far away from the cantilever resonance frequency. The AC amplitude was swept from 0 to 5 V (0.5 V step; 0 V direct current bias) while the tip was anchored in the selected suspension area. The responsive out-of-plane piezoelectric vibration causes deflection of the AFM tip, resulting in cantilever displacement. The vertical deflection of the cantilever is measured using a lock-in amplifier and reflected in the final output as amplitude and phase changes during PFM imaging. The quantitative vertical piezoelectric displacement induced by the out-of-plane electric field is represented by the piezoelectric coefficient, d_{33}. In PFM characterization, inhomogeneous electric field and other electrostatic effects might affect the actual measurement.[5,60] Thus, the measured piezoresponse coefficient should be defined as the effective piezoelectric coefficient,[5,19,61–64] d_{33}^{eff}, due to possible factors that affect the PFM measurements. The degree of polarization could be further reflected by the d_{33}^{eff} coefficient. The d_{33}^{eff} coefficient can be written as

$$d_{33}^{eff} = \frac{V_p(\text{mV}) \times \sigma(\text{nm V}^{-1})}{V_{AC}(\text{V})} = \frac{A_P(\text{pm})}{V_{AC}(\text{V})} \quad (9)$$

where A_p (pm) is the driven piezoelectric response displacement, V_p is the detected vertical deflection voltage, σ is the deflection sensitivity *versus* the cantilever and V_{AC} is the amplitude of the applied AC driving voltage.[61,65]

Fig. 6a presents the out-of-plane piezoelectric response images of monolayer MoS_2 under the driving voltage of 0, 1, 2, and 3 V. The amplitude values of the out-of-plane piezoelectric response along the diameter of the hole under different driving voltages is shown in Fig. S7 (ESI†). In the absence of driving voltage (V_{AC} = 0 V), there is no difference in piezoelectric response mapping between the supported and suspended areas. However, there is a weak piezoelectric response at the hole edge, which is attributed to the topography cross-talk caused by the steep morphology. Under non-zero driving voltage, there is a distinct piezoresponse amplitude variation between the curved and flat MoS_2 films. As the driving bias increases, the piezoresponse amplitude changes negligibly in the flat MoS_2 region, while the amplitude steadily increases in the curved region.

The average of the piezoresponse amplitudes in the selected regions of supported and suspended monolayer MoS_2 was plotted

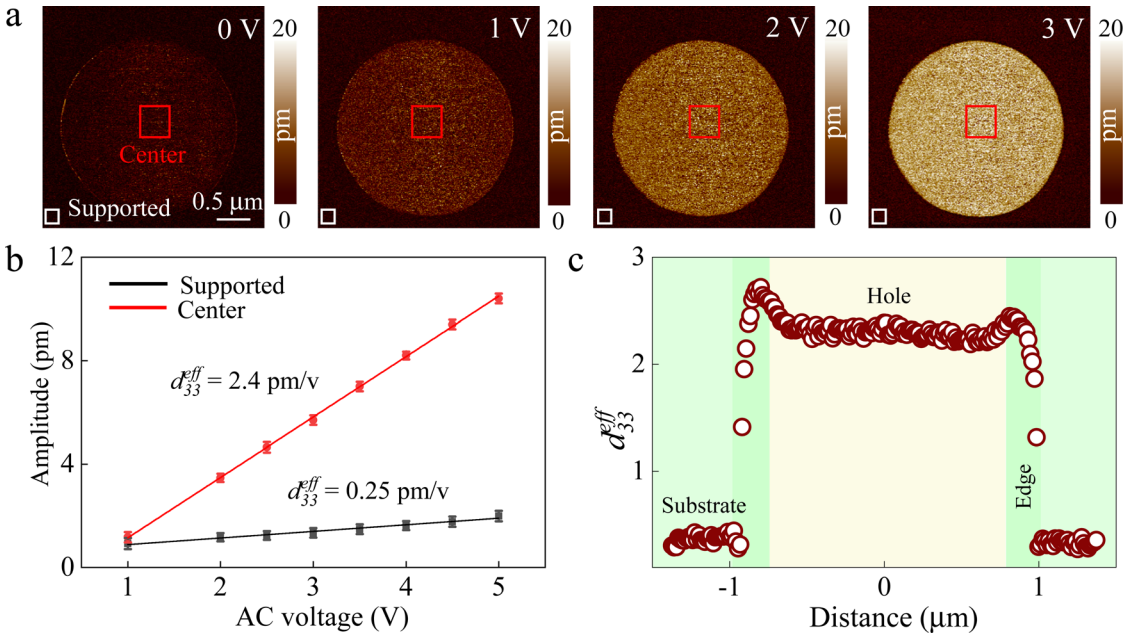

Fig. 6 (a) Out-of-plane piezoelectric response image of monolayer MoS_2 under the driving voltage of 0, 1, 2, and 3 V. (b) Average piezoresponse amplitude of supported and suspended monolayer MoS_2 under different voltages. A solid line is obtained by least squares fitting. (c) d_{33}^{eff} coefficients along the hole diameter as a function of r/R.

as a function of the applied AC voltage as shown in Fig. 6b. The value of d_{33}^{eff} is determined from the ratio of the driving piezoresponse displacement to the driving voltage. Thus, the d_{33}^{eff} coefficient of the supported and suspended areas can be directly obtained by calculating the slope of the linear-fitting curve in Fig. 6b. The d_{33}^{eff} value of the bent zone is significantly larger than that of the flat area, which is ascribed to the flexoelectricity induced by the strain gradient.[10,62] Although the supported MoS_2 film has no intrinsic out-of-plane piezoelectricity, a small d_{33}^{eff} coefficient is still measured to be 0.25 pm V^{-1}. A very weak d_{33}^{eff} coefficient is observed on the supported flake, which is due the substrate effect.

In PFM measurements, due to the bending of 2D materials, the projection in the z direction of intrinsic in-plane piezoelectric response may also be collected in addition to the response originated from the flexoelectric effect. Through rough calculation, it can be found that the projection of the intrinsic in-plane piezoelectric coefficient (d_{11}) along the z direction has very little contributions to the measured effective out-of-plane piezoelectric coefficient. The cross-section of curved 2D materials can be equivalent to a circular arc, as presented in Fig. S8 (ESI†). The projection in the z direction of the intrinsic in-plane piezoelectric coefficient is defined as d_{11-z}, and it follows $d_{11-z} = d_{11}\sin\theta$. Obviously, the projection in the z direction of the intrinsic in-plane piezoelectric coefficient (d_{11-z}) is maximum at the end point (point E) and zero at the center (point C). Thus, the measured d_{33}^{eff} (about 2.4 pm V^{-1}) at the center of bent-MoS_2 is mainly the contribution of flexoelectric polarization. In our experiment, Fig. 3b presents that the depth and radius of the curved MoS_2 film are approximately 116.56 nm and 2.36 μm, respectively. Geometrically, it is easy to conclude that the maximum value of $\sin\theta$ is about 0.1 at point E. Theoretically, the intrinsic in-plane piezoelectric coefficient (d_{11}) of 2D MoS_2 is maximum at the single layer, which is about 3.37 pm V^{-1}.[66] Hence, the maximum of d_{11-z} is less than 0.337 pm V^{-1} at the point E, which is negligible compared to the measured d_{33}^{eff} (about 2.8 pm V^{-1}) at the edge of bent MoS_2 flakes. Thereby, it can be concluded that the d_{33}^{eff} coefficient of bent 2D MoS_2 flakes is dominantly contributed by the flexoelectric effect, rather than the intrinsic in-plane piezoelectricity.

The d_{33}^{eff} coefficients along the hole diameter as a function of r/R are plotted in Fig. 6c. On flat monolayer MoS_2 films, the measured d_{33}^{eff} coefficient is almost constant. Obviously, the d_{33}^{eff} coefficient of the curved region with flexoelectricity is greater than that of the flat region. In addition, the value of the d_{33}^{eff} coefficient in the curved area fluctuates slightly, suggesting the regular distribution of total in-plane strain from bent flakes. For monolayer MoS_2, the d_{33}^{eff} constant is obtained as

$$d_{33}^{eff} = \frac{\mu_{11}}{c_{11}}\frac{\frac{\partial \varepsilon_p}{\partial z}}{\varepsilon_p}. \quad (10)$$

The calculation method and specific values of $\frac{\partial \varepsilon_p}{\partial z}$ are given in Table S1 (see ESI†). The ε_p distribution of monolayer MoS_2 is shown in Fig. 4f. For the case of $-0.858 < \frac{r}{R} < -0.429$, the strain gradient is 0.0038% nm^{-1}, while ε_p increases in the negative direction. In this case, the value of $\frac{\frac{\partial \varepsilon_p}{\partial z}}{\varepsilon_p}$ decreases, resulting in a diminishing trend of d_{33}^{eff}. Similarly, when the r/R range evolves from −0.429 to 0, the strain gradient is 0.0032% nm^{-1} and ε_p decreases in the negative direction. The increase in d_{33}^{eff} is attributed

Table 3 Longitudinal flexoelectric coefficient of thin-layered MX2 flakes

Material	Number of layers (n)	Radiusof hole (R [μm])	Bending depth H_{max} [nm]	Curvature K [10^{-2} μm^{-1}]	Strain gradient (%/μm)	ε_p^{bottom} (%)	$(c_{11}\varepsilon_p^{bottom})/n$ (10^8 pa)	μ_{11} (μC m^{-1})
MoS_2	1	2.36	116.56	4.2	3.5	0.35	0.093	0.061 (0.065[a])
		3.34	163.26	3.0	2.5	0.34	0.091	0.058
		5.50	280.89	1.9	1.5	0.38	0.100	0.066
	3	5.60	260.07	1.6	1.2	0.31	0.026	0.019
		4.94	210.95	1.7	1.3	0.26	0.021	0.017
		3.28	160.69	3.0	2.0	0.35	0.029	0.024
WSe2	1	4.72	190.42	1.7	1.3	0.24	0.040	0.030 (0.026[a])
	3	1.59	63.84	5.0	4.8	0.24	0.013	0.0084
		2.17	96.57	4.1	3.7	0.29	0.016	0.010
	5	2.24	106.17	4.2	4.2	0.37	0.012	0.0074
		3.49	189.79	3.1	2.4	0.48	0.016	0.0082
WS_2	1	5.63	267.26	1.7	1.9	0.33	0.090	0.049 (0.053[a])
		3.40	166.63	2.9	3.2	0.36	0.098	0.054
		5.10	265.21	2.0	2.3	0.41	0.112	0.060
		3.40	162.45	2.8	3.0	0.32	0.087	0.050
	2	5.10	194.61	1.5	1.7	0.21	0.028	0.015
		3.40	112.80	2.0	2.1	0.16	0.022	0.013
		5.67	204.39	1.3	1.4	0.19	0.026	0.014
	4	5.02	174.07	1.4	1.4	0.18	0.011	0.0067
		3.40	150.30	2.6	2.7	0.28	0.017	0.0074
	5	4.90	158.70	1.3	1.4	0.15	0.0073	0.0045
		3.28	105.85	2.0	1.9	0.15	0.0071	0.0043
		5.58	185.89	1.2	1.1	0.16	0.0076	0.0047
MoSe2	1	3.56	259.04	4.1	4.0	0.77	0.136	0.140 (0.103[a])
		3.60	213.20	3.3	3.4	0.51	0.090	0.116
	2	5.83	366.25	2.1	2.0	0.57	0.051	0.063
		5.20	398.01	2.9	3.1	0.85	0.075	0.076
	3	3.60	129.02	2.0	2.0	0.19	0.014	0.015
		5.20	208.61	1.5	1.4	0.23	0.017	0.021
		3.60	120.20	1.8	2.0	0.16	0.012	0.014
		5.20	154.08	1.1	0.9	0.13	0.0095	0.010
	5	5.83	166.75	1.0	1.1	0.12	0.0053	0.006
		5.20	153.24	1.1	0.8	0.13	0.0056	0.0062
		5.20	165.98	1.2	1.3	0.15	0.0066	0.0072
		5.78	162.02	1.0	1.0	0.11	0.0051	0.0056

[a] The prediction of the order-of-magnitude of the flexoelectric coefficient for monolayer $MoSe_2$, WS_2, and WSe_2 in ref. 5 and 19.

to an increase in $\frac{\partial \varepsilon_p}{\varepsilon_p}$. For monolayer WSe_2, WS_2, and $MoSe_2$ flakes, the d_{33}^{eff} values along the hole diameter were plotted as a function of r as shown in Fig. S9–S11 (ESI†). The fluctuation of d_{33}^{eff} coefficients also present a strong correlation with the distribution of ε_p.

Combining the strain distribution and d_{33}^{eff} coefficient, μ_{11} coefficients of the bent monolayer MX_2 films could be determined, as listed in Table 3. According to eqn (5), μ_{11} follows the rule

$$\mu_{11} = \frac{c_{11} d_{33}^{eff} \varepsilon_p}{\frac{\partial \varepsilon_p}{\partial z}}. \quad (11)$$

The elastic coefficient of monolayer MoS_2 is c_{11} = 265 GPa.[67] The μ_{11} coefficient of the monolayer curved MoS_2 film could be obtained by substituting the value of d_{33}^{eff}, ε_p and $\frac{\partial \varepsilon_p}{\partial z}$. For a monolayer MoS_2 flake with a curvature of 0.042 μm^{-1}, the μ_{11} coefficient is measured to be 0.061 μC m^{-1}, which is consistent with the reported experimental results.[5,19] In addition, μ_{11} constants of monolayer $MoSe_2$, WS_2, and WSe_2 films are further quantified, which are in agreement well with the predicted order-of-magnitude.[5,19] Therefore, it indicates that the μ_{11} coefficient of bent flakes could be measured reliably by combining the determined strain distribution and the obtained d_{33}^{eff} coefficient. Similarly, the μ_{11} coefficient of few-layered MX_2 films was further investigated. Table 3 presents the specific values of hole diameter, bending depth, curvature and the μ_{11} coefficient of few-layered flakes. Obviously, when the total

in-plane strain is similar, the μ_{11} coefficient decreases significantly with the number of layers grown. The strain and thickness dependence of the μ_{11} coefficient in few-layered films is here further discussed in the following.

Thickness tuning longitudinal flexoelectric constants

By combining *in situ* micro-Raman spectroscopy and PFM techniques, the μ_{11} coefficient could not only be obtained in bent monolayer films, but also be determined in few-layered systems. Here, the μ_{11} constants of thin-layered MX_2 flakes with different thickness and bending states were further verified. The basic microscopic characterization images of few-layered 2D flakes are shown in Fig. S12 (ESI†). We take WSe_2 flakes as an example to present the details of obtaining the μ_{11} coefficient of few-layered bent films. Fig. S13 (ESI†) displays the optical and AFM images of few-layered WSe_2 flakes suspended on porous substrates. For few-layered bent van der Waals materials, it is difficult to construct an atomistic calculation model, with complicated interactions between layers. Due to theoretical restrictions, the μ_{11} coefficient of monolayer bent films has been reported,[15,16] while the μ_{11} coefficient of few-layered curved flakes has never been investigated so far. The μ_{11} constants of WSe_2 flakes with a thickness of 2.78 nm and 4.23 nm under different flexural conditions are observed. Taking WSe_2 films with a thickness of 4.23 nm as an example, the distribution of strain and d_{33}^{eff} coefficient along the hole diameter of few-layered films was presented.

We first observed the biaxial strain distribution of the WSe_2 membrane with a thickness of 4.23 nm. The basic microscopic and AFM topography maps of WSe_2 films with a radius of nearly 2.2 μm and a flexural depth of about 106.2 nm are shown in Fig. S13a and b (ESI†). The suspended few-layered WSe_2 flakes presented an analogous geometry with bent monolayer WSe_2 films. Raman spectra of few-layered WSe_2 films present three characteristic peaks. The prominent broad peak at 250 μm^{-1} is a combination of the double degenerate E_{2g} mode and A_{1g} mode.[68] The A_{1g} mode is an out-of-plane mode, in which the top and bottom chalcogen atoms vibrate in opposite directions. While the phonon mode of E_{2g} is in-plane, where metal atoms and chalcogen atoms vibrate in the antiphase. Because E_{2g} and A_{1g} modes entangle with each other and are difficult to distinguish, we define the degenerate peak at 250 cm^{-1} as E_{2g}/A_{1g}. There is also a signal around 260 cm^{-1} for thin-layered WSe_2 films, which could be regarded as a second order peak induced by a double resonance effect involving the LA phonons located around 130 cm^{-1} under no strain. In addition, it is noted that a weak signature emerges around 310 cm^{-1}, which can be

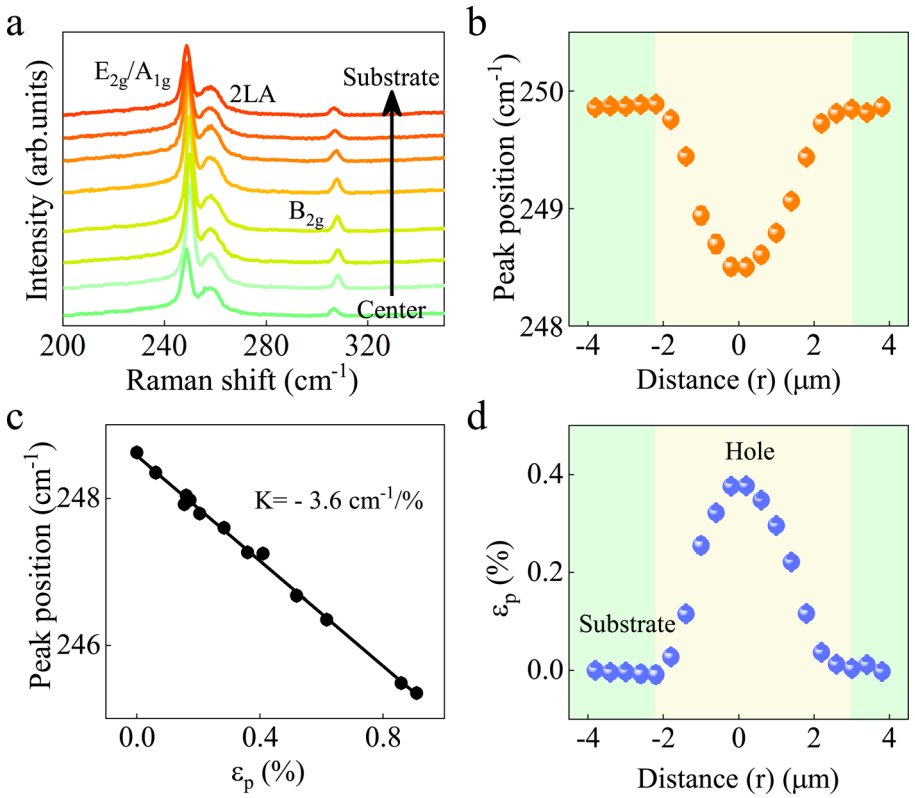

Fig. 7 (a) Raman spectra of five-layer WSe_2 flakes from the edge to the center along the diameter of holes. (b) Raman peak position of E_{2g}/A_{1g} as a function of *r*. The center of bent WSe_2 film is defined as $r = 0$. (c) Raman peak position of E_{2g}/A_{1g} as a function of biaxial strain. The black solid line is obtained by the least square fitting, and the fitted slope is $K = -3.6$ cm^{-1}/%. (d) Strain distribution diagram corresponding to the peak position distribution in panel (b).

reassigned to the normally inactive B_{2g} mode.[69] Fig. 7a displays Raman spectra of WSe_2 flakes from the edge to the center along the diameter of the hole. Interestingly, all phonon modes continuously soften to varied degrees from the substrate to center. This phenomenon indicates that the strain of thin-layered WSe_2 films varies continuously. The A_{1g} mode is more sensitive to biaxial strain. The shift in the degenerate peak position could more accurately reflect the strain distribution of few-layered WSe_2. Therefore, we extracted Raman frequency (peak position) of E_{2g}/A_{1g} as a function of r, as shown in Fig. 7b. The center of bent WSe_2 flakes is defined as $r = 0$. The peak position decreases nonlinearly from the edge to the hole center, presenting a centrally symmetric distribution. Around the center, the peak position reaches the minimum value, indicating that the strain is greatest at $r = 0$.

In order to further present the strain distribution of WSe_2 films, the shift rate of the E_{2g}/A_{1g} Raman mode with the total in-plane strain was measured. For WSe_2, the ν value is 0.192, and then $f(\nu) = 0.736$. Hence, the total in-plane strain at the center of WSe_2 flakes could be expressed as $\varepsilon_p^{bottom} = 1.472 \cdot \left(\frac{H_{max}}{R}\right)^2$. Raman spectra at the center of WSe_2 films with diverse diameters and different bending depths were recorded. The composite peak position of E_{2g}/A_{1g} modes is a function of the total in-plane strain, like those in Fig. 7c. The peak position of the degenerate mode shifted linearly with strain at a rate of -3.6 cm^{-1} $\%^{-1}$. Due to the large atomic mass of WSe_2, the frequency shift of the composite peak with total in-plane strain is not as significant as that in MoS_2. According to the shift rate of the peak position of the E_{2g}/A_{1g} mode with strain, the strain distribution of thin-layered suspended films could be obtained from the peak position distribution shown in Fig. 7b. Fig. 7d presents the total in-plane strain distribution along the diameter of the hole. The total in-plane strain increases nonlinearly from the edge and reaches the maximum value of 0.34% at the hole center, presenting a central-symmetric distribution. This result is in compliance with the spatial distribution of ε_p predicted by the finite-element method.[24] Namely, the approach of quantifying the total in-plane strain distribution according to the frequency shift of E_{2g}/A_{1g} is convincible and reliable. Similarly, this phenomenon was observed on few-layered MoS_2, WS_2, and $MoSe_2$ films, as presented in Fig. S14–S16 (ESI†). Peak positions of A_{1g} are central-symmetrical and reach a minimum at the center of the hole. Therefore, the ε_p of thin-layered flakes presents a similar spatial distribution.

The presence of a strain gradient from few-layered bent WSe_2 flakes also could induce additional electromechanical coupling response. PFM was utilized to reveal the distribution of effective out-of-plane electromechanical coupling of the same sample. Fig. S17 (ESI†) shows out-of-plane piezoelectric response of WSe_2 films with a thickness of 4.23 nm under increased drive voltages. The amplitude of out-of-plane piezoresponse along the diameter of the hole under different driving voltages can be seen in Fig. 8a. Without the bias modulation, a weak piezoelectric response is observed in the curved region, which may be due to the cross-talk caused by the variation of

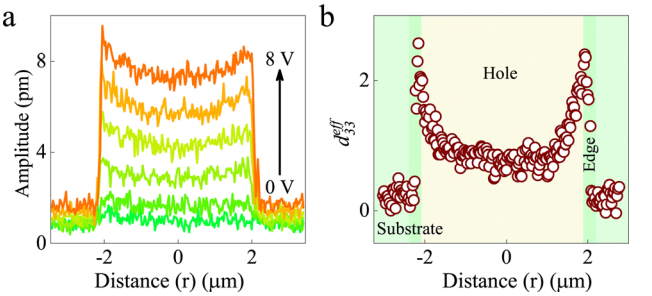

Fig. 8 (a) Amplitude of the out-of-plane piezoelectric response along the diameter of holes under 0–8 V driving voltages. (b) d_{33}^{eff} coefficient as a function of r along the hole diameter.

the topography. When an effective voltage is applied, a prominent piezoelectric amplitude response is observed in the bent areas of WSe_2 flake with a thickness of 4.23 nm. The out-of-plane piezoelectric amplitude diagram along the diameter of the hole manifests that the piezoresponse of curved WSe_2 films is much stronger than that of flat regions, and the amplitude increases linearly with the driving voltage. It is worth noting that the piezoelectric amplitude in thde flat area scarcely changes with increasing driving bias. It is attributed to no dipole moment induced by the strain gradient in the flat MoS_2 region, despite the existence of an external electric field.

The d_{33}^{eff} constant could be quantified using the linear-fitting slope of the piezoelectric response amplitude as a function of applied AC voltage. According to the slope of the fitted curve at each point in the amplitude profile, the distribution of the d_{33}^{eff} coefficient along the hole diameter can be obtained, as illustrated in Fig. 8b. The d_{33}^{eff} coefficient of the flat region is close to zero and almost unchanged. Significantly, the d_{33}^{eff} coefficient of the curved region is obviously larger than that of the supported area, and presents a regular fluctuation. This fluctuation of the d_{33}^{eff} coefficient is related to the symmetrical distribution of ε_p from bent thin-layered WSe_2. According to the calculation of the strain gradient (see the ESI†), the value of $\frac{\partial \varepsilon_p}{\partial z}$ is determined to be 0.0042% nm^{-1}, as listed in Table 3. When the strain gradient is constant, the d_{33}^{eff} coefficient is inversely proportional to ε_p. For the case of $-2 < r < -1$, ε_p increases nonlinearly, which leads to a nonlinear decrease in d_{33}^{eff}. ε_p remains almost unchanged for the case of $-1 < r < 1$, and d_{33}^{eff} also displays a similar trend. When the range of r is from 1 to 2, d_{33}^{eff} nonlinearly increases, due to the nonlinear reduction of ε_p.

The μ_{11} constant of bent WSe_2 films with the elastic coefficient of 163 GPa[67] and a curvature of 0.042 μm^{-1} is determined to be 0.0074 $\mu C\ m^{-1}$ by combining the strain distribution and d_{33}^{eff}. In order to further investigate the related factors to determine the flexoelectric coefficient, the μ_{11} constants of MX_2 flakes with diverse thicknesses and the various curvature degrees were studied. The elastic coefficients of few-layered 2D films are shown in Table S2 (see ESI†). Table 3 presents all specific values of hole diameter, bending depth of curved flakes, strain gradient, and the μ_{11} coefficient of thin-layered

MX_2 films with diverse thicknesses. In addition, we highlight the comparison of the measured flexoelectric constants on 2D flakes in Table 3, considering the reported data and this work. In our work, the μ_{11} constant of few-layered MX_2 flakes was determined. It is worth noting that the μ_{11} coefficient is sensitive to thickness.

According to the measured monolayer height of about 0.8–1.1 nm as reported in,[10] the number of layers could be summarized in Table 3. The curvature of thin-layered flakes (K) is approximately equal to the strain gradient, $\frac{\partial \varepsilon_p}{\partial z} \approx K = \frac{1}{\alpha}$. Hence, the universal formula for calculating the μ_{11} coefficient of curved 2D materials can be further simplified as eqn (6). Furthermore, for the same material, the measured d_{33}^{eff} coefficient is proportional to the reciprocal of the product of thickness and curvature radius in our previous work,[10] $d_{33}^{eff} \propto \frac{1}{n\alpha}$. Therefore, the μ_{11} of a bent film can be derived as

$$\mu_{11} = \alpha d_{33}^{eff} c_{11} \varepsilon_p \propto \alpha \frac{1}{n\alpha} c_{11} \varepsilon_p \propto c_{11} \varepsilon_p \frac{1}{n} \propto c_{11} \varepsilon_p^{bottom} \frac{1}{n}. \quad (12)$$

The values of μ_{11} and $(c_{11}\varepsilon_p^{bottom})/n$ of the curved few-layered 2D flakes are given in Table 3. Significantly, for identical materials, μ_{11} is proportional to $(c_{11}\varepsilon_p^{bottom})/n$. The results verify that the flexoelectric coefficient of a bent film is proportional to the product of the aspect ratio and reciprocal of thickness. Namely, tuning both the aspect ratio of films $\left(\frac{H_{max}}{R}\right)$ and thickness can be regarded as a valid approach to regulate the bending flexoelectric coefficient of 2D materials.

Conclusion

In this work, a general formula (eqn (6)) for calculating the μ_{11} coefficients of free-standing 2D materials is proposed for the first time, which is modified from the calculation of the flexoelectric effect for bulk dielectric materials. According to the d_{33}^{eff} coefficient formula (eqn (5)) of the bent film, the expression of the flexoelectric coefficient (eqn (6)) is confirmed. According to the formula, the μ_{11} coefficient of free-standing thin-layered 2D flakes was experimentally measured by the *in situ* PFM technique with confocal Raman spectroscopy. Position dependent peak frequency of the curved films by micro-Raman scattering is used to quantify the biaxial strain distribution in the bent 2D films on a nanoscale, according to the shift rate of peak position with strain. The strain gradient, namely, $\frac{\partial \varepsilon_p}{\partial z}$, is obtained from the shift rate of strain with the displacement in the z direction. From the scanning height map of the suspended film along the diameter of the hole, the value of z corresponding to each ε_p could be obtained. Through the *in situ* PFM technique, the d_{33}^{eff} coefficient of the curved 2D flakes is further determined. Combining ε_p, $\frac{\partial \varepsilon_p}{\partial z}$ and d_{33}^{eff} coefficient, the μ_{11} coefficient of bent films could be further quantified.

By this universal formula, we have experimentally measured the μ_{11} constant of the bent MX_2 flakes on a nanoscale. Near the centers of the curved 2D films, the total in-plane strain reaches maximum values and presents a central-symmetrical distribution, indicating the gradient distribution of strain. Moreover, flexoelectric polarization induced by the strain gradient in few-layered MX_2 flakes was observed and quantified using *in situ* PFM. The d_{33}^{eff} coefficient in the bending region shows a regular distribution related to strain. Combining the strain and d_{33}^{eff} coefficient distribution, the μ_{11} coefficient of monolayer bent MoS_2 films was determined to be about 0.061 μC m^{-1}, which is consistent with the experimental prediction. In addition, μ_{11} constants of monolayer $MoSe_2$, WS_2, and WSe_2 films are further quantified, which is in agreement well with the experimentally predicted order-of-magnitude. Furthermore, the formula could be used to further determine the μ_{11} constant of thin-layered flakes. More importantly, the μ_{11} constant of bent 2D materials has been verified to be proportional to the product of the aspect ratio and the reciprocal of thickness. In other words, the value of the μ_{11} coefficient could be manipulated by tuning the aspect ratio and thickness of flakes. The present work gives a physical method for quantifying the flexoelectric coefficient, which could effectively prevent theoretical constraints, promoting further understanding of the flexoelectric properties of atomically thin 2D materials and the development and application of potential flexoelectric devices.

Materials and methods

Preparation of porous substrates

In order to obtain a large and stable strain gradient while avoiding the interference of substrate effects on test results, we expect to obtain non-destructive 2D materials with suspended structures. It is a relatively simple and efficient method to construct suspended 2D materials through patterned substrates with hole structures. The mechanical structure of the suspended atomic-thick film on a circular hole is more stable. In addition, the strain distribution of suspended films is also highly symmetrical, which is easy to analyze. Therefore, we choose a patterned substrate with a circular hole matrix structure.

Electron beam lithography (EBL, Pioneer Two, Raith) technique was used to prepare porous substrates in this experiment. The process of preparing the hole matrix patterned substrate is as follows. First, a polymethyl methacrylate (PMMA) photoresist with a thickness of 300–350 nm was spin-coated on a cleaned conductive substrate. After spin-coating PMMA, electron beam exposure was performed according to a pre-designed pattern. After the exposure is completed, the developing and fixing steps are carried out. The exposed photoresist is dissolved in the developer, leaving hole structures on the substrate. In order to improve surface properties of the substrate, a gold film with a thickness of 50 nm was coated on the PMMA surface using a thermal evaporator. Therefore, holes with diameter of 3–11 μm and depth of 250–300 nm were obtained on the substrate.

Sample preparation

Monolayer and few-layer MX_2 flakes were obtained by mechanical exfoliation of bulk MX_2 crystals. The 2D material prepared by mechanical exfoliation can be directly transferred on the porous substrate by a dry transfer method to obtain the suspended 2D films. The specific steps of the dry transfer method are as follows. First, MX_2 crystals were thinned with the assistance of scotch tape. With the help of polydimethylsiloxane (PDMS), thin crystals were removed from the scotch tape and thinned again.[70] The suitable 2D films were observed and selected using an optical microscope. Finally, the selected samples were transferred to the prefabricated hole matrix substrate with the assistnce of a 2D material directional transfer auxiliary platform, and suspended 2D flakes can be obtained.

Characterization methods

A confocal micro-Raman spectrometer (Jobin-Yvon LabRAM HR Evolution, Horiba) with an excitation laser of 532 nm was used to analyze the suspended MX_2 flakes. The beam of a 532 nm laser was focused using a 100x objective lens, and the laser power was less than 1 mW. Utilizing a commercial AFM system (Dimension Icon, Bruker), the ''ScanAsyst-air'' tip was used to characterize the morphology and thickness of 2D flakes. NanoScope software was used for data acquisition and analysis. A conductive ''SCM-PIT'' tip coated with Pt/Lr was used to detect piezoelectric response by PFM in the contact mode. The tip radius of the ''SCM-PIT'' tip is about 20 nm, the force constant is around 2.8 N m^{-1}, and the resonance frequency is approximately 75 kHz. The applied *AC* voltage frequency was selected to be 15 kHz, effectively avoiding the contact resonance of the tip-sample junction, whose contact resonance frequency is above 300 kHz. The piezoresponse amplitudes at each measurement point along the hole diameter was extracted as a function of the applied AC voltage by the MATLAB program. The value of d_{33}^{eff} is determined from the ratio of the driving piezoresponse displacement to the driving voltage. Therefore, the d_{33}^{eff} coefficients along the hole diameter can be directly obtained by calculating the slope of the linear fit curve at each measuring point.

Author contributions

M. Deng, A. Cui, and Z. Hu initiated and designed the experiments and wrote the manuscript. M. Deng, X. Wang, K. Jiang and X. Xu discussed PFM and Raman data. M. Deng, J. Zhang and L. Zhu conducted device fabrication experiments. Y. Li, L. Shang and J. Chu gave the detailed analyses of the underlying mechanism. All the authors contributed to the manuscript preparation.

Conflicts of interest

There are no conflicts to declare.

Acknowledgements

This work was financially supported by the National Natural Science Foundation of China (grant no. 62090013, 61974043, 12104156, 62074058, and 61974044), the National Key R&D Program of China (grants no. 2019YFB2203403), the Projects of Science and Technology Commission of Shanghai Municipality (grant no. 21JC1402100 and 19511120100), the China Postdoctoral Science Foundation (grants no. 2020TQ0099 and 2020M681222), the Natural Science Foundation of Chongqing, China (CSTB2022NSCQ-MSX1367), and the Program for Professor of Special Appointment (Eastern Scholar) at Shanghai Institutions of Higher Learning and Shanghai Pujiang Program (20PJ1403600).

References

1 T. Ikeda, *Fundamentals of Piezoelectricity*, Oxford University Press, 1996.
2 W. Heywang, K. Lubitz and W. Wersing, *Piezoelectricity: Evolution and Future of a Technology*, Springer Series in Materials Science, Springer Science & Business Media, 2008, vol. 114.
3 X. Wang, H. Tian, W. Xie, Y. Shu, W.-T. Mi, M. A. Mohammad, Q.-Y. Xie, Y. Wang, J.-B. Xu and T.-L. Ren, *NPG Asia Mater.*, 2015, **7**, e154.
4 X. Song, F. Hui, T. Knobloch, B. Wang, Z. Fan, T. Grasser, X. Jing, Y. Shi and M. Lanza, *Appl. Phys. Lett.*, 2017, **111**, 083107.
5 C. J. Brennan, R. Ghosh, K. Koul, S. K. Banerjee, N. Lu and E. T. Yu, *Nano Lett.*, 2017, **17**, 5464–5471.
6 X.-Q. Zheng, J. Lee and P. X.-L. Feng, *Microsyst. Nanoeng.*, 2017, **3**, 17038.
7 M. Zelisko, Y. Hanlumyuang, S. Yang, Y. Liu, C. Lei, J. Li, P. M. Ajayan and P. Sharma, *Nat. Commun.*, 2014, **5**, 4284.
8 M. N. Blonsky, H. L. Zhuang, A. K. Singh and R. G. Hennig, *ACS Nano*, 2015, **9**, 9885–9891.
9 S. I. Kundalwal, S. A. Meguid and G. J. Weng, *Carbon*, 2017, **117**, 462–472.
10 X. Wang, A. Y. Cui, F. F. Chen, L. P. Xu, Z. G. Hu, K. Jiang, L. Y. Shang and J. H. Chu, *Small*, 2019, **15**, 1903106.
11 S. K. Kim, R. Bhatia, T. H. Kim, D. Seol, J. H. Kim, H. Kim, W. Seung, Y. Kim, Y. H. Lee and S. W. Kim, *Nano Energy*, 2016, **22**, 483–489.
12 W. Z. Wu, L. Wang, Y. L. Li, F. Zhang, L. Lin, S. M. Niu, D. Chenet, X. Zhang, Y. F. Hao, T. F. Heinz, J. Hone and Z. L. Wang, *Nature*, 2014, **514**, 470–474.
13 S. V. Kalinin and V. Meunier, *Phys. Rev. B: Condens. Matter Mater. Phys.*, 2008, **77**, 033403.
14 A. G. Kvashnin, P. B. Sorokin and B. I. Yakobson, *J. Phys. Chem. Lett.*, 2015, **6**, 2740–2744.
15 X. Y. Zhuang, B. He, B. Javvaji and H. S. Park, *Phys. Rev. B*, 2019, **99**, 054105.
16 B. Javvaji, B. He, X. Y. Zhuang and H. S. Park, *Phys. Rev. Mater.*, 2019, **3**, 125402.
17 S. Kumar, D. Codony, I. Arias and P. Suryanarayana, *Nanoscale*, 2021, **13**, 1600–1607.
18 D. Codony, I. Arias and P. Suryanarayana, *Phys. Rev. Mater.*, 2021, **5**, L030801.

19 C. J. Brennan, K. Koul, N. Lu and E. T. Yu, *Appl. Phys. Lett.*, 2020, **116**, 053101.
20 H. Y. Zhu, Y. Wang, J. Xiao, M. Liu, S. M. Xiong, Z. J. Wong, Z. L. Ye, Y. Ye, X. B. Yin and X. Zhang, *Nat. Nanotechnol.*, 2015, **10**, 151–155.
21 K. Lefki and G. J. M. Dormans, *J. Appl. Phys.*, 1994, **76**, 1764.
22 V. Nagarajan, *Appl. Phys. Lett.*, 2005, **87**, 242905.
23 D. Lloyd, X. H. Liu, J. W. Christopher, L. Cantley, A. Wadehra, B. L. Kim, B. B. Goldberg, A. K. Swan, J. S. Bunch and J. Scott, *Nano Lett.*, 2016, **16**, 5836–5841.
24 E. Blundo, C. D. Giorgio, G. Pettinari, T. Yildirim, M. Felici, Y. Lu, F. Bobba and A. Polimeni, *Adv. Mater. Interfaces*, 2020, **7**, 2000621.
25 K. Yue, W. Gao, R. Huang and K. M. Liechti, *J. Appl. Phys.*, 2012, **112**, 083512.
26 D. Tedeschi, E. Blundo, M. Felici, G. Pettinari, B. Q. Loi, T. Yildrim, E. Petroni, C. Zhang, Y. Zhu, S. Sennato, Y. R. Liu and A. Polimeni, *Adv. Mater.*, 2019, **31**, 1903795.
27 E. Blundo, M. Felici, T. Yildrim, G. Pettinari, D. Tedeschi, A. Miriametro, B. Liu, W. Ma, Y. Lu and A. Polimeni, *Phys. Rev. Res.*, 2020, **2**, 012024.
28 M. Luo, Z. H. Zhang and B. I. Yakobson, *J. Appl. Mech.*, 2013, **80**, 040906.
29 P. Johari and V. B. Shenoy, *ACS Nano*, 2012, **6**, 5449–5456.
30 W. B. Fichter, *NASA Tech. Pap.*, 1997, **3658**, 1–24.
31 D. Cakir, F. M. Peeters and C. Sevik, *Appl. Phys. Lett.*, 2014, **104**, 203110.
32 S. P. Koenig, N. G. Boddeti, M. L. Dunn and J. S. Bunch, *Nat. Nanotechnol.*, 2011, **6**, 543–546.
33 L. E. Cross, *J. Mater. Sci.*, 2006, **41**, 53–63.
34 T. D. Nguyen, S. Mao, Y. W. Yeh, P. K. Purohit and M. C. McAlpine, *Adv. Mater.*, 2013, **25**, 946–974.
35 Y. Sun, S. E. Thompson and T. Nishida, *Strain Effect in Semiconductors: Theory and Device Applications*, Springer, 2010, ch. 2.
36 A. Jain, S. P. Ong, G. Hautier, W. Chen, W. D. Richards, S. Dacek, S. Cholia, D. Gunter, D. Skinner, G. Ceder and K. A. Persson, *APL Mater.*, 2013, **1**, 011002.
37 M. de Jong, W. Chen, T. Angsten, A. Jain, R. Notestine, A. Gamst., M. Sluiter, C. K. Ande, S. van der Zwaag, J. J. Plata, C. Toher, S. Curtarolo, G. Ceder, K. A. Persson and M. Asta, *Sci. Data*, 2015, **2**, 150009.
38 Y. Zhang, H. H. Guo, W. Sun, H. Z. Sun, S. Ali, Z. D. Zhang, R. Saito and T. Yang, *J. Raman Spectrosc.*, 2020, **51**, 1353–1361.
39 P. Umari, A. Pasquarello and A. Dal Corso, *Phys. Rev. B: Condens. Matter Mater. Phys.*, 2001, **63**, 094305.
40 M. Lazzeri and F. Mauti, *Phys. Rev. Lett.*, 2003, **90**, 036401.
41 A. P. Nayak, T. Pandey, D. Voiry, J. Liu, S. T. Moran, A. Sharma, C. Tan, C. H. Chen, L. J. Li, M. Chhowalla, J. F. Lin, A. K. Singh and D. Akinwande, *Nano Lett.*, 2015, **15**, 346–353.
42 H. Li, A. W. Contryman, X. Qian, S. M. Ardakani, Y. Gong, X. Wang, J. M. Weisse, C. H. Lee, J. Zhao, P. M. Ajayan, J. Li, H. C. Manoharan and X. Zheng, *Nat. Commun.*, 2015, **6**, 7381.
43 H. J. Conley, B. Wang, J. I. Ziegler, R. F. Haglund Jr., S. T. Pantelides and K. I. Bolotin, *Nano Lett.*, 2013, **13**, 3626–3630.
44 J. Zabel, R. R. Nair, A. Ott, T. Georgiou, A. K. Geim, K. S. Novoselov and C. Casiraghi, *Nano Lett.*, 2012, **12**, 617–621.
45 C. C. Xu, Q. Z. Yao, H. Z. Du, C. Y. Hong, T. Xue, Y. L. Kang and Q. Y. Li, *ACS Appl. Mater. Interfaces*, 2021, **13**, 22040–22046.
46 Y. L. Wang, C. X. Cong, C. Y. Qiu and T. Yu, *Small*, 2013, **9**, 2857–2861.
47 Y. Y. Hui, X. F. Liu, W. J. Jie, N. Y. Chan, J. H. Hao, Y. T. Hsu, L. J. Li, W. L. Guo and S. P. Lau, *ACS Nano*, 2013, **7**, 7126–7131.
48 C.-H. Chang, X. Fan, S.-H. Lin and J.-L. Kuo, *Phys. Rev. B: Condens. Matter Mater. Phys.*, 2013, **88**, 195420.
49 R. Proksch, *J. Appl. Phys.*, 2014, **116**, 66804.
50 J. S. Sekhon, L. Aggarwal and G. Sheet, *Appl. Phys. Lett.*, 2014, **104**, 162908.
51 Q. N. Chen, Y. Ou, F. Ma and J. Li, *Appl. Phys. Lett.*, 2014, **104**, 242907.
52 R. K. Vasudevan, N. Balke, P. Maksymovych, S. Jesse and S. V. Kalinin, *Appl. Phys. Rev.*, 2017, **4**, 21302.
53 D. Seol, B. Kim and Y. Kim, *Curr. Appl. Phys.*, 2017, **17**, 661–674.
54 B. Kim, D. Seol, S. Lee, H. N. Lee and Y. Kim, *Appl. Phys. Lett.*, 2016, **109**, 102901.
55 D. Seol, S. Kang, C. Sun and Y. Kim, *Ultramicroscopy*, 2019, **207**, 112839.
56 S. Kim, D. Seol, X. Lu, M. Alexe and Y. Kim, *Sci. Rep.*, 2017, **7**, 41657.
57 J. Shakya, S. Kumar, D. Kanjilal and T. Mohanty, *Sci. Rep.*, 2017, **7**, 9576.
58 S. V. Kalinin and A. N. Morozovska, *Nat. Nanotechnol.*, 2015, **10**, 917–918.
59 S. V. Kalinin and V. Meunier, *Phys. Rev. B: Condens. Matter Mater. Phys.*, 2008, **77**, 033403.
60 T. Jungk, Á. Hoffmann and E. Soergel, *Nano Energy*, 2007, **86**, 353–355.
61 N. Syed, A. Zavabeti, J. Z. Ou, M. Mohiuddin, N. Pillai, B. J. Carey, B. Y. Zhang, R. S. Datta, A. Jannat, F. Haque, K. A. Messalea, C. L. Xu, S. P. Russo, C. F. McConville, T. Daeneke and K. Kalantar-Zadeh, *Nat. Commun.*, 2018, **9**, 3618.
62 S. Kang, S. Jeon, S. Kim, D. Seol, H. Yang, J. Lee and Y. Kim, *ACS Appl. Mater. Interfaces*, 2018, **10**, 27424–27431.
63 E. N. Esfahani, T. Li, B. Huang, X. D. Xu and J. Y. Li, *Nano Energy*, 2018, **52**, 117–122.
64 Y. C. Wang, L. M. Vu, T. Lu, C. L. Xu, Y. Liu, J. Z. Ou and Y. X. Li, *ACS Appl. Mater. Interfaces*, 2020, **12**, 51662–51668.
65 M. H. Zhao, Z. L. Wang and S. X. Mao, *Nano Lett.*, 2004, **4**, 587–590.
66 K.-A. N. Duerloo, M. T. Ong and E. J. Reed, *J. Phys. Chem. Lett.*, 2012, **3**, 2871–2876.
67 N. Iguiñiz, R. Frisenda, R. Bratschitsch and A. Castellanos-Gomez, *Adv. Mater.*, 2019, **31**, 1807150.
68 H. Terrones, E. Del Corro, S. Feng, J. M. Poumirol, D. Rhodes, D. Smirnov, N. R. Pradhan, Z. Lin, M. A. T. Nguyen,

A. L. Elias, T. E. Mallouk, L. Balicas, M. A. Pimenta and M. Terrones, *Sci. Rep.*, 2014, **4**, 4215.
69 P. Tonndorf, R. Schmidt, P. Böttger, X. Zhang, J. Börner, A. Liebig, M. Albrecht, C. Kloc, O. Gordan, D. R. T. Zahn, S. Michaelis de Vasconcellos and R. Bratschitsch, *Opt. Express*, 2013, **21**, 4908–4916.
70 Y. Huang, E. Sutter, N. N. Shi, J. B. Zheng, T. Z. Yang, D. Englund, H. J. Gao and P. Sutter, *ACS Nano*, 2015, **9**, 10612–10620.